Polylactic acid-based patterned matrixes for site-specific delivery of neuropeptides on-demand: functional NGF effects on human neuronal cells

1 **Olga A. Sindeeva,**[*,1] **Olga Kopach,**[*,2] **Maxim A. Kurochkin,**[3] **Andrei Sapelkin,**[4] **David J. Gould,**[5]
2 **Dmitri A. Rusakov**[#,2] **and Gleb B. Sukhorukov**[#,6]

3 [1]Remote Controlled Theranostic Systems Lab, Department of Nanotechnology, Educational and
4 Research Institute of Nanostructures and Biosystems, Saratov State University, Saratov, Russia

5 [2]UCL Queen Square Institute of Neurology, University College London, London, United Kingdom

6 [3]Center for Photonics and Quantum Materials, Skolkovo Institute of Science and Technology,
7 Moscow, Russia

8 [4]School of Physics and Astronomy, Queen Mary University of London, London, United Kingdom

9 [5] Biochemical Pharmacology, William Harvey Research Institute, Queen Mary University of London,
10 London, United Kingdom

11 [6]School of Engineering and Material Science, Queen Mary University of London, London, United
12 Kingdom

13 **#Correspondence:** d.rusakov@ucl.ac.uk; g.sukhorukov@qmul.ac.uk

14 * These authors have contributed equally to this work

17 **Abstract**

18 The patterned microchamber arrays based on biocompatible polymers are a versatile cargo delivery
19 system for drug storage and site- and time specific drug release on demand. However, functional
20 evidence of their action on nerve cells, in particular their potential for enabling patterned neuronal
21 morphogenesis, remains unclear. Recently, we have established that the polylactic acid (PLA)-based
22 microchamber arrays are biocompatible with human cells of neuronal phenotype and provide safe
23 loading for hydrophilic substances of low molecular weight, with successive site-specific cargo release
24 on-demand to trigger local cell responses. Here, we load the nerve growth factor (NGF) inside
25 microchambers and grow N2A cells on the surface of patterned microchamber arrays. We find that the
26 neurite outgrowth in local N2A cells can be preferentially directed towards opened microchambers
27 (site-specific NGF release). These results suggest the PLA-microchambers can be an efficient drug

delivery system for the site- and time-specific delivery of neuropeptides, potentially suitable for guidance of human nerve cells.

1   Introduction

Micro- and nanostructured matrices have prompted new lines of study focusing on cell behavior (adhesion, proliferation, morphology, alignment, migration, gene expression, and even differentiation) and tissue engineering (Sousa et al., 2019). Photolithography and electroplating technique allows creation of templates with different geometries suitable for reusable synthesis of the patterned films composed of polymers, proteins and colloids with nanoscale fidelity.

Among the large number of biomaterials thus obtained, patterned microchamber array (MCA) (Kiryukhin et al., 2018; Zykova et al., 2019) are of particular importance. The capability of loading biologically active substances into microchambers (microcontainers) allows modulated cell function, not only due to the periodic structure of the material (Norman and Desai, 2006; Bettinger et al., 2009; Ge et al., 2015; Sousa et al., 2019), but also due to the encapsulated cargo release (Kopach et al., 2019). A wide range of biocompatible polymers for the MCA synthesis enables control of the cargo release rate. For example, it was shown that the polylactic acid (PLA)-based microchambers reliably retain dye for several days (Gai et al., 2017). PLA-based microchambers start relatively slow spontaneous release of adrenaline hydrochloride from the first day after entering the aqueous environment (Sindeeva et al., 2018a), which has a clear advantage in many clinical applications. The release of significant quantity of cargo can be induced by ultrasound as a result of simultaneous opening of many microchambers (Sindeeva et al., 2018a), or otherwise individual chambers can be opened by optical laser targeting (Gai et al., 2018; Kopach et al., 2019; Kurochkin et al., 2020).

Notwithstanding the advantages of MCA as a system for targeted delivery of drugs and biologically active substances, its applications in human cells remain poorly understood, which precludes further clinical use of these systems. This is mainly because the methods of encapsulation, the duration of storage, the release rate of the substance depend not only on the shell material (Lee and Yeo, 2015) and container geometry (Macha et al., 2019), but also on the cargo chemical and physical properties (Albinali et al., 2019), which vary widely for each specific substance. Earlier, we demonstrated that PLA-based MCA are fully biocompatible with human cells of neuronal phenotype. In addition, we showed a site-specific cellular response to the release of a low-molecular weight neurotransmitter from individual microchambers by two-photon laser irradiation (Kopach et al., 2019). Here, we demonstrate the possibility of neuronal cell function modulation through loading and site-specific release of the nerve growth factor (NGF).

2   Materials and Methods

The laser-triggered drug release of encapsulated NGF from MCA to the targeted N2A cells cultivated on the MCA surface was performed using focused near-infrared (NIR) laser light with wavelength of 830 nm. NGF is a neuropeptide, which makes this substance particularly sensitive to small temperature fluctuations. The use of the NIR laser is explained by minimal absorption of biological tissues in a 650 - 975 nm spectral range, which will reduce the impact of laser-caused photothermal effects on NGF, N2A cells or on another potential tissue. Additionally the localisation of the laser-triggered photothermal influence on the chamber wall was ensured by the inclusion of gold nanoparticles (GNPs)

68 in the shells of microchambers as photoabsorbing agents (Wijaya et al., 2009; Agarwal et al., 2011).
69 GNPs is a safe (Sperling et al., 2008; Boisselier and Astruc, 2009), well-established, and widely used
70 thermosensitive material for polymer carrier opening, *in vitro* and *in vivo* (Radt et al., 2004; Skirtach
71 et al., 2005; Boisselier and Astruc, 2009; Singh, 2010; Kunzmann et al., 2011)**.**

2.1   Materials

73 For MCA synthesis biopolymer polylactide acid (PLA, 3 mm granule, molecular weight 60,000),
74 chloroform and Nerve Growth Factor-β (molecular weight 13,5 kDa) were purchased from Sigma-
75 Aldrich (UK). The Poly(dimethylsiloxane) (PDMS) kit (Sylgard 184) was purchased from Dow-
76 Corning (Midland, USA).

77 For gold nanorods (GNRs) synthesis, cetyltrimethylammonium bromide (CTAB, >98.0 %),
78 hydrochloric acid (HCl, 37 wt % in water), L-ascorbic acid (>99.9 %), and sodium borohydride
79 ($NaBH_4$, 99 %) were purchased from Sigma-Aldrich (UK). Hydrogen tetrachloroaurate trihydrate
80 ($HAuCl_4 \cdot 3H_2O$) and silver nitrate ($AgNO_3$, >99 %) were purchased from Alfa Aesar.

2.2   Synthesis of GNRs

82 GNRs were fabricated by the modified seed-mediated method (Nikoobakht and El-Sayed, 2003;
83 Khlebtsov et al., 2011) At the first step, the seed solution was obtained by mixing 250 μL of 10 mM
84 $HAuCl_4$ and 10 mL of 0,1 M CTAB. The ice-cold 10 mM NaBH4 was added to the mixture in the
85 volume of 1 mL. At the second step, 10 mL of the seed solution were mixed with 900 μL of 0.1 M
86 CTAB, 20 mL of 4 mM $AgNO_3$, 50 mL of 10 mM $HAuCl_4$, 10 mL of 1 M HCl, and 10 mL of 0.1 M
87 ascorbic acid for preparing GNRs. Then nanorods were centrifuged at 12000 g for 60 min. The pellet
88 was re-suspended in deionized water. The final solution was containing about 1012 GNRs per mL;
89 their average width was 11 ± 3 nm and length was 40 ± 6 nm. The axial ratio was ~3.8, according the
90 longitudinal resonance was ~790 nm.

2.3   Fabrication of PLA-based MCA and NGF loading

92 The silicon master was previously made at Shenzhen Semiconductor (Shenzhen, China) using
93 photolithography for MCA synthesis. The pattern on silicon master was represented by plate with
94 185000 cylinders equidistant from each other (diameter of 10 μm, height 4 μm, and distance from
95 center to center of 20 μm). For the synthesis of patterned films the PDMS stamp was made as a reverse
96 impression from a silicone master from a mixture of the prepolymer and curing agent (10:1 ratio). The
97 mixture was degassed for 30 minutes in vacuum and consolidated (at 70 °C for 3 hours). After this,
98 PDMS master was cut out and separated from the silicon master. The shell of PLA-based MCA was
99 made by sealing (printing) of two films: the patterned and the flat ones (2 kg cm^{-2}, 15 seconds, at 55
100 °C). For synthesis of the patterned film, the PDMS stamp with microwells was dip-coated for 5 seconds
101 into the 1 wt% PLA chloroform solution, for obtaining the flat PLA microfilm the same procedure was
102 made with cover glass. After printing, the PDMS stamp was removed and MCA was located on cover
103 glass.

104   The patterned film was covered with GNRs before printing, by scattering GNRs on the inner surface
105   of the PLA film by sedimentation (Sindeeva et al., 2018b). As a result, aggregates of gold nanoparticles
106   were visualized with an optical microscope, as well as with scanning electron microscopy (SEM) and
107   transmission electron microscopy (TEM).

108   NGF loading was carried out by applying 10 µl of an aqueous solution (10 µg/mL) on the inner surface
109   of the patterned film after the deposition of GNRs. For homogeneous loading, the solution was evenly
110   distributed over the entire film surface and allowed to completely dry.

111   2.4   Laser-induced opening of individual PLA-based microchambers

112   Laser-induced opening of individual PLA microchambers with N2A cells growing on the top of the
113   MCA surface was performed using a home-made system. A detailed description of the system and the
114   procedure are presented below in the Results section (3.3).

115   2.5   SEM and TEM techniques

116   To visualize MCA morphology at different steps through the fabrication procedure (payload, sealing)
117   and after opening microchamber(s), SEM was used to ensure appropriate samples (FEI Quanta ESEM,
118   electron microscope, FEI, Hillsboro, USA). SEM was carried out using an accelerating voltage of 10
119   kV, a spot size of 3.5, and a working distance of approximately 10 mm.

120   TEM images of the MCA with GNRs were obtained using a Jeol 2100 microscope (Tokyo, Japan).
121   GNRs diameters and lengths were evaluated from digitized TEM images (Grapher 8, Golden Software,
122   Inc.) of about 500 GNRs.

123   2.6   Human N2A cell culture

124   For testing functional effects of the laser-triggered release of NGF from PLA-microchambers, we used
125   human N2A cells. The cell line was maintained as we have recently described in detail (Kopach et al.,
126   2019). Briefly, N2A cells were cultured in Dulbecco's modified Eagle medium (DMEM, Invitrogen,
127   Carlsbad, CA, USA), supplemented with 2 mM L-glutamine and 10% fetal bovine serum, 2%
128   penicillin-streptomycin, and 1% non-essential amino acids at 37 °C (5% CO_2). After harvesting, cells
129   were washed out and plated on a surface of PLA-based MCA, pre-treated with UV light for at least 2
130   h in advance. For cell differentiation to neuronal phenotype the culturing medium was low serum (2%)
131   DMEM. Microscopic images of differentiating N2A cells on the fabricated MCA were collected before
132   microchamber opening and then afterwards at various time-points. For the time-lapse imaging, a MCA
133   with differentiating N2A cells on its surface was placed in a microscope cage incubator (5 cm^2 Petri
134   dish) to maintain experimental conditions favorable for live cell imaging (37 °C, 5% CO_2). Images
135   were acquired every 10 min for up to 60 hours total.

136   In separate experiments, N2A cells were plated on glass coverslips placed into a 8 x 8 wells-plate.
137   Experimental groups consisted of the cells of the same passage grown on glass in culture medium
138   without NGF or NGF supplemented at the concentration of 10 ng/ml or 100 ng/ml. There were typically
139   four independent samples tested for each experimental group.

2.7   Assessment of neurite length; cell density analysis

Neurite outgrowth by N2A cells was assessed by measuring the neurite length in different experimental conditions, using a NeuronJ, a plugin of ImageJ software (NIH, Bethesda, USA). Neurites were traced in individual cells manually, using variable digital zooming. Analyses were performed in the cell culture field of view, across multiple areas selected in a pseudo-random manner.

The N2A cell density was analyzed by counting cell bodies on the surface of the fabricated array, within the area of interest (close to the opened microchambers). Cell density was estimated as the number of viable cells per mm^2 over the selected period of time-lapse recording, as indicated.

2.8   Statistical analysis

Data are presented as mean ± standard error of the mean, with n referring to the number of neurites measured for their length, for each experimental group. To determine statistical difference between experimental groups, two-tailed unpaired Student's t-test was used. A p value of less than 0.05 was considered as an indicator of the statistically significant difference.

3   Results and discussion

3.1   PLA-based MCA with gold nanoparticles: fabrication and characterization

MCA was created by printing the flat and patterned films (Figure 1A). The thickness of the finished film was 0.8−1.0 μm. GNPs (as a classical method) were included in the MCA composition before printing, to enable controlled opening of microchambers with laser light (Singh, 2010; Kunzmann et al., 2011)

[Figure 1 about here. Double column fitting image]

For surface modification, a priori concentrated water solution with GNRs was prepared (200 mg/mL). 200 μL of this solution was placed on the inner surface of the patterned microfilm with microwells, for 3 h. During this time, the patterned film was horizontally oriented, after which the drop was removed using a micropipette. The entire surface of the patterned film was covered with GNR aggregates, which were clearly visible under an optical microscope. Figure 1 shows an SEM image (D) and TEM image (E) of the GNR aggregates location. For precipitation and sedimentation of GNRs, 200 μL of 0.5 M NaCl solution was added to 200 μL of the nanoparticles solution to enhance aggregation (Madzharova et al., 2018). The resulting solution was centrifuged at 10,000 rpm, and supernatant was removed. Next, GNRs were resuspended in 200 μL of deionized water. After that procedure, aggregates of GNRs started to adsorb on a hydrophobic PLA surface. Aggregates in comparison with non-aggregated particles have a larger size and mass which leads to amplification of sedimentation rate (Midelet et al., 2017). GNRs content in the patterned film was 0.47 pg/μm^2, as estimated from the absorption spectrum change in the solution, before and after deposition of aggregates.

3.2   NGF loading

5

174 Microchambers were filled by applying 10 µL of the NGF solution (concentration 10 µg/mL) on the
175 patterned PLA film surface (8.5x8.5 mm, 185000 microwells), before printing it on a flat film.
176 Although the PLA film has hydrophobic properties (Alakrach et al., 2018), the NGF solution uniformly
177 wetted the patterned surface due to the low surface tension. The drying of the NGF solution occurred
178 evenly over the entire film surface, with a gradual decrease of the solution drop thickness (Figure 2A).
179 When the water layer thickness reached a critical point, the rapid formation of crystals in the wells
180 began over the entire surface (Figures 2A and C). The crystallization process could be clearly observed
181 in a light microscope in real time (Video in Supplemental Information).

182   [Figure 2 about here. Double column fitting image]

183 The images obtained using SEM confirmed the uniformity of filling the microwells with crystals, and
184 the absence of NGF between them (Figure 3).

185   [Figure 3 about here. Double column fitting image]

186 In general, the amount of NGF was 100 ng per sample (8.5x8.5 mm) and 0.54 pg per microchamber.
187 This amount was calculated theoretically, by taking into account the total amount of substance depleted
188 on the patterned film surface, and the number of microwells.

189 **3.3   Individual microchamber opening using 830 nm laser**

190 We developed a new optical system to enable individual microchambers opening and cells
191 visualization. The in-house-made system was based on an inverted microscope (Olympus ix71, Japan),
192 into the optical path of which we integrated a continuous-wave (CW) near-infrared (NIR) laser module
193 (LD830-MA1W, 830 nm, maximum optical power 1W, Thorlabs Inc. USA) with adjustable output
194 power, to enable selected chambers photo-thermal activation (Figure 4A). First, NIR laser light was
195 collimated by an aspheric lens, and was 3x expanded by an anamorphic prism pair. Next, laser light
196 was directed into the microscope infinity port by the two-mirror periscope. Then, the laser light was
197 directed by an infrared short-pass dichroic mirror (DMSP805, 805 nm cutoff wavelength, Thorlabs
198 Inc., USA) into an exit pupil of an infinity-corrected objective lens LCAch 20x/0.4 PhC (Olympus,
199 Japan), and focused by the objective into a 1 µm spot on the surface of a selected microchamber, at a
200 power of 15 mW over 0.5 s. The laser light irradiation exposure time was controlled by a mechanical
201 shutter. The N2A cells reaction to a local NGF release was registered using monochrome CMOS sensor
202 (DCC3260M, Thorlabs Inc., USA) with infrared filter. The NIR lasers are widely used for the opening
203 of targeted drug delivery systems which is associated with precise beam focusing and good penetration
204 ability in tissue without damages of living cells.

205 The exposure to laser light (Figure 4B) was accompanied by the appearance of a small gas bubble
206 (Figure 4C) and by structural changes of the microchamber surface (Figure 4D). The bubble formation
207 is associated with the liquid boiling on GNRs surface as a result of energy absorption and fast plasma
208 formation occurring after liquid evaporation and subsequent vapor expansion, which are accompanied
209 by a shock wave (Lauterborn and Ebeling, 1977; Baghdassarian et al., 1999; Link et al., 2000; Link
210 and El-Sayed, 2001). NIR lasers are used for heating up GNRs in the polymer shell because GNRs
211 efficiently absorb laser energy (Gordel et al., 2014). The heating of light absorber agents such as GNRs

212 by laser irradiation leads also to the rapid melting of the carrier walls, and subsequent cargo release
213 (Radt et al., 2004; Skirtach et al., 2005, 2007; Singh, 2010).

214 [Figure 4 about here. Double column fitting image]

3.4 Directed neurite outgrowth by local N2A cells towards the opened microchambers with NGF payload inside

217 Here, we sought to test functional effects of NGF following the laser-triggered opening of
218 microchambers. We utilized the human N2A cell line, a cell type providing a fast cell growth and
219 differentiation to neuronal phenotype of human origin, as shown previously (Kopach et al., 2019). As
220 expected, differentiating N2A cells developed typical axon-like processes and numerous neurites 1 d
221 post-plating (Figure 5A), which could extend up to 50 μm in length, with morphogenesis progressing
222 during cell growth.

223 First, we evaluated the NGF-induced effects on differentiating N2A cells grown on glass (control
224 group). Since NGF displaysactivity in the ng/mlconcentration range , we supplemented NGF to culture
225 medium at the concentration of 10 ng/ml and 100 ng/ml. There was a clear, dose-dependent effect of
226 NGF on the neurite outgrowth by N2A cells observed after 1 day of cell differentiation with NGF
227 (Figure 5C-D). The neurite length was on average ~31.1 μm in control (0 NGF, n = 666 neurites), but
228 ~40.3 μm in the presence of 10 ng/ml NGF (n = 541 neurites; $p < 0.0001$) and ~46.8 μm with 100
229 ng/ml NGF (n = 544 neurites, $p < 0.0001$; Figure 5B) for N2A cells of the same passage.

230 [Figure 5 about here. Double column fitting image]

231 Next, we placed N2A cells on the surface of the fabricated MCA with NGF payload inside
232 microchambers, and grew the cells on MCA (Figure 6A). The cells showed no signs of toxicity of the
233 fabricated MCA, consistent with the previously reported biocompatibility of PLA as the constituent
234 material (Kopach et al., 2019). We monitored N2A cells before and after laser-triggered opening of
235 microchambers, throughout the area of interest for a few days. We could observe that after
236 microchamber opening, the cell density increased within the targeted area (Figure 6B), and local cells
237 extended their neurites towards the opened microchambers (Figure 6A). These effects were observed
238 across 6 independent experiments (fabricated MCA / cell preparations), at the day 1 or 2 after opening.
239 The effect was observed regardless of trajectory applied for microchamber opening: a line segment
240 (Figure 6A), or sequence of line followed by rectangular or square shape (Figure 7A). Apparently the
241 heat required to open MCA did not destroy NGF since the heat is generated locally.

242 [Figure 6 about here. Double column fitting image]

243 Finally, we carried out time-lapse recording of differentiating N2A cells before and after opening
244 microchambers with NGF payload by collecting images from the area of interest every 10 min, for up
245 to 3 days in total (Figure 7). We traced the increased cell density within the targeted area, with a sharp
246 rise in the cell density in response to each sequence of microchamber opening (3 times, ~20 hours
247 apart) (Figure 7B). On a finer scale, cells growing in close proximity to the opened microchambers
248 directed their neurites towards the sites of NGF release from opened microchambers (Figure 7, images

249 on an expanded scale). These results demonstrate a directed neurite outgrowth by the on demand site-
250 targeted cargo release from PLA-microchambers.

251   [Figure 7 about here. Double column fitting image]

Conclusion

253 The patterned PLA-based MCA are a versatile drug delivery system for site-specific, geometrically
254 constrained cargo release on demand. We confirm that the PLA-based matrix is fully biocompatible
255 with human-derived cells, which is particularly important for highly sensitive cells of neuronal
256 phenotype. Microchambers provide safe loading for hydrophilic peptidesand, because of the presence
257 of gold nanoparticles in the container shell, provide site-specific cargo release on demand. Optical
258 targeting of microchambers for drug release has triggered functional cell responses locally.
259 Importantly, N2A cells demonstrate enhanced neurite outgrowth towards individual microchambers
260 releasing NGF. The PLA-based MCA are therefore a potentially suitable platform for site-specific
261 targeting of neuronal cells of human origin.

Data Availability

263 The raw data supporting the conclusions of this manuscript will be made available by the authors,
264 without undue reservation, to any qualified researcher.

Author Contributions

266 **OAS, OK, MAK, AS, NVT, DAR** and **GBS** contributed conception and design of the study. **GBS,**
267 **DAR, OAS, OK, MAK** - experiment design and manuscript writing, **OAS, OK, MAK -** conducting
268 experiments, **OK** - cells state statistical analysis, **MAK** and **AS -** design and development of optical
269 system for chambers activation, **DJG** – discussions, **DAR** and **GBS -** guidance of the project. All
270 authors contributed to manuscript revision, read, and approved the submitted version.

Funding

Acknowledgments

278 **Conflict of Interest Statement**

279 The authors declare that the research was conducted in the absence of any commercial or financial
280 relationships that could be construed as a potential conflict of interest.

281 **References**

282 Agarwal, A., Mackey, M. A., El-Sayed, M. A., and Bellamkonda, R. V. (2011). Remote Triggered
283   Release of Doxorubicin in Tumors by Synergistic Application of Thermosensitive Liposomes
284   and Gold Nanorods. *ACS Nano* 5, 4919–4926. doi:10.1021/nn201010q.

285 Alakrach, A. M., Noriman, N. Z., Dahham, O. S., Hamzah, R., Alsaadi, M. A., Shayfull, Z., et al.
286   (2018). Chemical and Hydrophobic Properties of PLA/HNTs-ZrO 2 Bionanocomposites. *J.*
287   *Phys. Conf. Ser.* 1019, 012065. doi:10.1088/1742-6596/1019/1/012065.

288 Albinali, K., Zagho, M., Deng, Y., and Elzatahry, A. (2019). A perspective on magnetic core–shell
289   carriers for responsive and targeted drug delivery systems. *Int. J. Nanomedicine* Volume 14,
290   1707–1723. doi:10.2147/IJN.S193981.

291 Baghdassarian, O., Tabbert, B., and Williams, G. A. (1999). Luminescence Characteristics of Laser-
292   Induced Bubbles in Water. *Phys. Rev. Lett.* 83, 2437–2440. doi:10.1103/PhysRevLett.83.2437.

293 Bettinger, C. J., Langer, R., and Borenstein, J. T. (2009). Engineering Substrate Topography at the
294   Micro- and Nanoscale to Control Cell Function. *Angew. Chemie Int. Ed.* 48, 5406–5415.
295   doi:10.1002/anie.200805179.

296 Boisselier, E., and Astruc, D. (2009). Gold nanoparticles in nanomedicine: preparations, imaging,
297   diagnostics, therapies and toxicity. *Chem. Soc. Rev.* 38, 1759. doi:10.1039/b806051g.

298 Gai, M., Frueh, J., Kudryavtseva, V. L., Yashchenok, A. M., and Sukhorukov, G. B. (2017).
299   Polylactic Acid Sealed Polyelectrolyte Multilayer Microchambers for Entrapment of Salts and
300   Small Hydrophilic Molecules Precipitates. *ACS Appl. Mater. Interfaces* 9, 16536–16545.
301   doi:10.1021/acsami.7b03451.

302 Gai, M., Kurochkin, M. A., Li, D., Khlebtsov, B. N., Dong, L., Tarakina, N., et al. (2018). In-situ
303   NIR-laser mediated bioactive substance delivery to single cell for EGFP expression based on
304   biocompatible microchamber-arrays. *J. Control. Release* 276, 84–92.
305   doi:10.1016/j.jconrel.2018.02.044.

306 Ge, X., Leng, Y., Lu, X., Ren, F., Wang, K., Ding, Y., et al. (2015). Bacterial responses to periodic
307   micropillar array. *J. Biomed. Mater. Res. Part A* 103, 384–396. doi:10.1002/jbm.a.35182.

308 Gordel, M., Olesiak-Banska, J., Matczyszyn, K., Nogues, C., Buckle, M., and Samoc, M. (2014).
309   Post-synthesis reshaping of gold nanorods using a femtosecond laser. *Phys. Chem. Chem. Phys.*

16, 71–78. doi:10.1039/C3CP53457J.

Khlebtsov, B., Khanadeev, V., Pylaev, T., and Khlebtsov, N. (2011). A New T-Matrix Solvable
Model for Nanorods: TEM-Based Ensemble Simulations Supported by Experiments. *J. Phys. Chem. C* 115, 6317–6323. doi:10.1021/jp2000078.

Kiryukhin, M. V., Lau, H. H., Goh, S. H., Teh, C., Korzh, V., and Sadovoy, A. (2018). A membrane film sensor with encapsulated fluorescent dyes towards express freshness monitoring of packaged food. *Talanta* 182, 187–192. doi:10.1016/j.talanta.2018.01.085.

Kopach, O., Zheng, K., Sindeeva, O. A., Gai, M., Sukhorukov, G. B., and Rusakov, D. A. (2019). Polymer microchamber arrays for geometry-controlled drug release: a functional study in human cells of neuronal phenotype. *Biomater. Sci.* 7, 2358–2371. doi:10.1039/C8BM01499J.

Kurochkin, M. A., Sindeeva, O., Brodovskaya, E. P., Gai, M., Frueh, J., Su, L., Sapelkin, A., Tuchin, V. V., and Sukhorukov, G. B. (2020). Laser-triggered drug release from polymeric 3-D micro-structured films via optical fibers. *Mater. Sci. and Eng.: C,* 110664. doi:10.1016/j.msec.2020.110664.

Kunzmann, A., Andersson, B., Thurnherr, T., Krug, H., Scheynius, A., and Fadeel, B. (2011). Toxicology of engineered nanomaterials: Focus on biocompatibility, biodistribution and biodegradation. *Biochim. Biophys. Acta - Gen. Subj.* 1810, 361–373. doi:10.1016/j.bbagen.2010.04.007.

Lauterborn, W., and Ebeling, R. (1977). High-speed holography of laser-induced breakdown in liquids. *Appl. Phys. Lett.* 31 (10), 663–664.

Lee, J. H., and Yeo, Y. (2015). Controlled drug release from pharmaceutical nanocarriers. *Chem. Eng. Sci.* 125, 75–84. doi:10.1016/j.ces.2014.08.046.

Link, S., Burda, C., Nikoobakht, B., and El-Sayed, M. A. (2000). Laser-Induced Shape Changes of Colloidal Gold Nanorods Using Femtosecond and Nanosecond Laser Pulses. *J. Phys. Chem. B* 104, 6152–6163. doi:10.1021/jp000679t.

Link, S., and El-Sayed, M. A. (2001). Spectroscopic determination of the melting energy of a gold nanorod. *J. Chem. Phys.* 114 (5), 2362–2368.

Macha, I. J., Ben-Nissan, B., Vilchevskaya, E. N., Morozova, A. S., Abali, B. E., Müller, W. H., et al. (2019). Drug Delivery From Polymer-Based Nanopharmaceuticals—An Experimental Study Complemented by Simulations of Selected Diffusion Processes. *Front. Bioeng. Biotechnol.* 7. doi:10.3389/fbioe.2019.00037.

Madzharova, F., Heiner, Z., Simke, J., Selve, S., and Kneipp, J. (2018). Gold Nanostructures for Plasmonic Enhancement of Hyper-Raman Scattering. *J. Phys. Chem. C* 122, 2931–2940. doi:10.1021/acs.jpcc.7b10091.

344 Midelet, J., El-Sagheer, A. H., Brown, T., Kanaras, A. G., and Werts, M. H. V. (2017). The
345   Sedimentation of Colloidal Nanoparticles in Solution and Its Study Using Quantitative Digital
346   Photography. *Part. Part. Syst. Charact.* 34, 1700095. doi:10.1002/ppsc.201700095.

347 Nikoobakht, B., and El-Sayed, M. A. (2003). Preparation and Growth Mechanism of Gold Nanorods
348   (NRs) Using Seed-Mediated Growth Method. *Chem. Mater.* 15, 1957–1962.
349   doi:10.1021/cm020732l.

350 Norman, J. J., and Desai, T. A. (2006). Methods for Fabrication of Nanoscale Topography for Tissue
351   Engineering Scaffolds. *Ann. Biomed. Eng.* 34, 89–101. doi:10.1007/s10439-005-9005-4.

352 Radt, B., Smith, T. A., and Caruso, F. (2004). Optically Addressable Nanostructured Capsules. *Adv.*
353   *Mater.* 16, 2184–2189. doi:10.1002/adma.200400920.

354 Sindeeva, O. A., Gusliakova, O. I., Inozemtseva, O. A., Abdurashitov, A. S., Brodovskaya, E. P.,
355   Gai, M., et al. (2018a). Effect of a Controlled Release of Epinephrine Hydrochloride from
356   PLGA Microchamber Array: In Vivo Studies. *ACS Appl. Mater. Interfaces* 10, 37855–37864.
357   doi:10.1021/acsami.8b15109.

358 Sindeeva, O. A., Prikhozhdenko, E. S., Bratashov, D. N., Vostrikova, A. M., Atkin, V. S., Ermakov,
359   A. V., et al. (2018b). Carbon dot aggregates as an alternative to gold nanoparticles for the laser-
360   induced opening of microchamber arrays. *Soft Matter* 14, 9012–9019.
361   doi:10.1039/C8SM01714J.

362 Singh, S. (2010). Nanomedicine–Nanoscale Drugs and Delivery Systems. *J. Nanosci. Nanotechnol.*
363   10, 7906–7918. doi:10.1166/jnn.2010.3617.

364 Skirtach, A. G., Dejugnat, C., Braun, D., Susha, A. S., Rogach, A. L., Parak, W. J., et al. (2005). The
365   Role of Metal Nanoparticles in Remote Release of Encapsulated Materials. *Nano Lett.* 5, 1371–
366   1377. doi:10.1021/nl050693n.

367 Skirtach, A. G., Déjugnat, C., Braun, D., Susha, A. S., Rogach, A. L., and Sukhorukov, G. B. (2007).
368   Nanoparticles Distribution Control by Polymers: Aggregates versus Nonaggregates. *J. Phys.*
369   *Chem. C* 111, 555–564. doi:10.1021/jp065635k.

370 Sousa, M. P., Arab-Tehrany, E., Cleymand, F., and Mano, J. F. (2019). Surface Micro- and
371   Nanoengineering: Applications of Layer-by-Layer Technology as a Versatile Tool to Control
372   Cellular Behavior. *Small* 15, 1901228. doi:10.1002/smll.201901228.

373 Sperling, R. A., Rivera Gil, P., Zhang, F., Zanella, M., and Parak, W. J. (2008). Biological
374   applications of gold nanoparticles. *Chem. Soc. Rev.* 37, 1896. doi:10.1039/b712170a.

375 Wijaya, A., Schaffer, S. B., Pallares, I. G., and Hamad-Schifferli, K. (2009). Selective Release of
376   Multiple DNA Oligonucleotides from Gold Nanorods. *ACS Nano* 3, 80–86.
377   doi:10.1021/nn800702n.

378 Zykova, Y., Kudryavtseva, V., Gai, M., Kozelskaya, A., Frueh, J., Sukhorukov, G., et al. (2019).
379   Free-standing microchamber arrays as a biodegradable drug depot system for implant coatings.
380   *Eur. Polym. J.* 114, 72–80. doi:10.1016/j.eurpolymj.2019.02.029.

Figure legends

Figure 1. A diagram of the MCA, with a drug cargo and GNRs (A). Typical SEM image of PLA-based MCA with GNRs (B). SEM images of PLA patterned film, without (C) and with GNR aggregates (D). The arrangement of GNR aggregates (E, TEM image).

Figure 2. Optical images of the patterned PLA film (A), showing the NGF crystallization process, and an empty patterned film (B), bright-field microscopy in phase contrast mode. The border of NGF solution drop is marked with a blue line. Schematic illustration of the NGF crystallization process on the patterned PLA film (C).

Figure 3. SEM images of NGF crystals inside the microwells on patterned PLA film.

Figure 4. A diagram illustrating the experimental design and the laser-induced opening of MCA with NGF loaded inside (A). Typical images of microchambers before (B) and after (C) laser exposure (bright-field microscopy). SEM image of an opened microchamber (D).
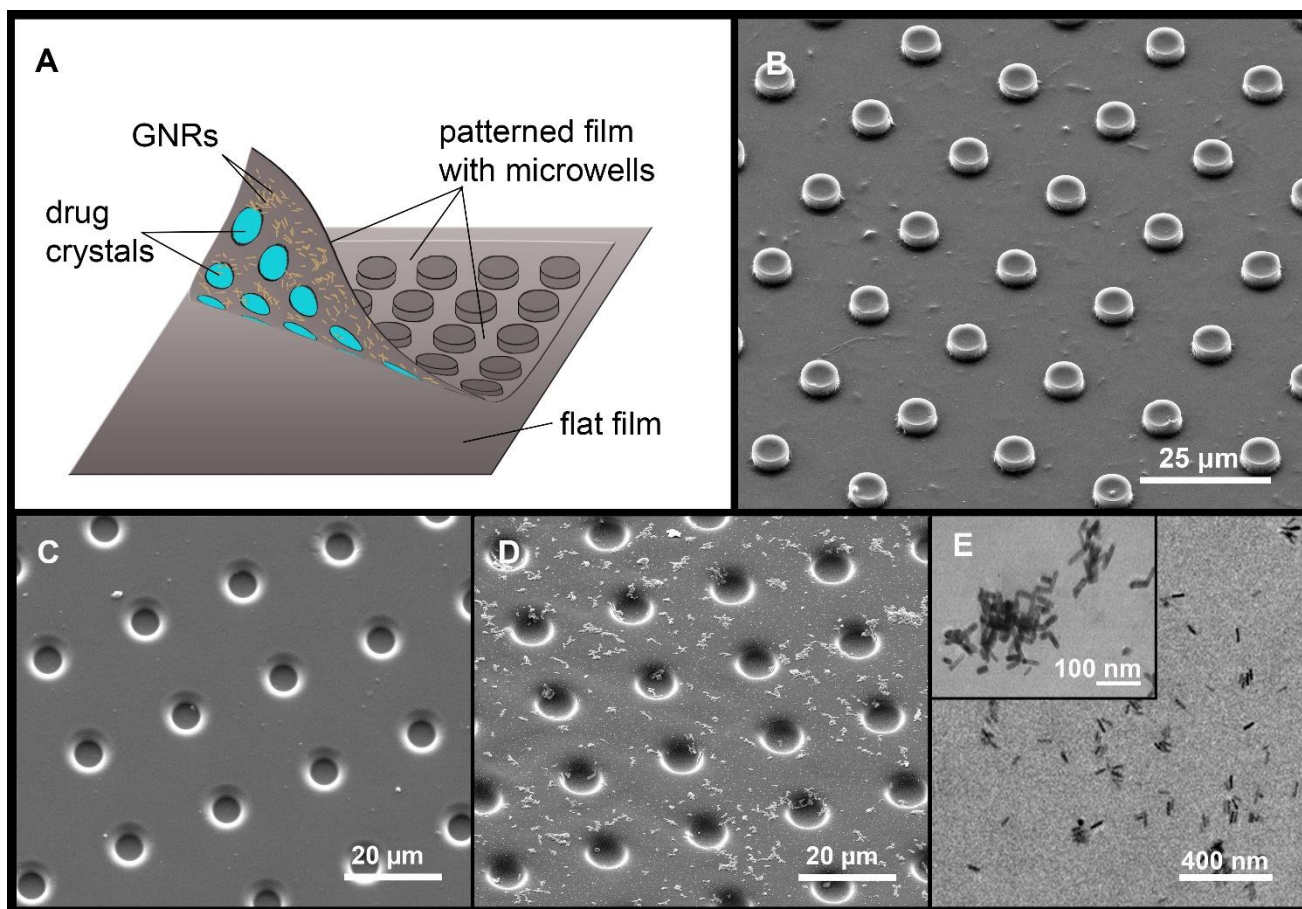
Figure 5. Dose-dependent effect of NGF on the neurite outgrowth in N2A cells on glass coverslips. A snapshot of differentiating N2A cells after 1 day of cell growth on glass (A). Statistical summary of the neurite length in N2A cells grown without or with NGF supplemented to culture medium at the concentration of 10 ng/ml or 100 ng/ml. Numbers of neurites measured for their length are indicated; at least four independent samples (coverslips) were tested for each group. ***$P < 0.001$ (two-tailed, unpaired t-test). (B) Representative images of differentiating N2A cells after 1 day of cell growth with NGF at different concentrations: 10 ng/ml (C) or 100 ng/ml (D).

Figure 6. Directed neurite outgrowth by local N2A cells and cell migration towards the laser-opened microchambers with NGF payload inside. (A) Representative snapshots of differentiating N2A cells growing on the surface of PLA-based MCA with NGF payload inside microchambers before microchamber opening (upper row) and 1 day after (lower row). Red dotted line, a line segment trajectory for optical targeting microchambers (7 microchambers opened). Red arrows, directed migration of individual cells from their original positions; green arrows, cell neurites directed toward the opened microchambers (NGF release). (B) Cell tracking diagrams depicting individual N2A cell positions before laser-triggered microchamber opening (top) and 1 day after (bottom). Note directed migration of local cells (red arrows) from their original positions toward the opened microchambers. Data are representative of images on (A).

Figure 7. Monitoring morphogenesis of differentiating N2A cells upon triggered, site-specific NGF release from PLA-microchambers. (A) Representative snapshots of differentiating N2A cells on the surface of MCA with NGF-loaded microchambers before and following laser-triggered microchamber opening at various time-points. Images taken from the same area of interest; red dotted lines and blue marks, trajectories for optical targeting (the sequence consists of varied trajectory for opening 3 times, ~20 hours apart). Scale bars, 40 µm. (B) Time-course of cell density changes within the targeted area during the time-lapse imaging (~60 hours total) before and following triggered NGF release from PLA-microchambers, shown on A. Red arrows, time of laser-triggered opening.
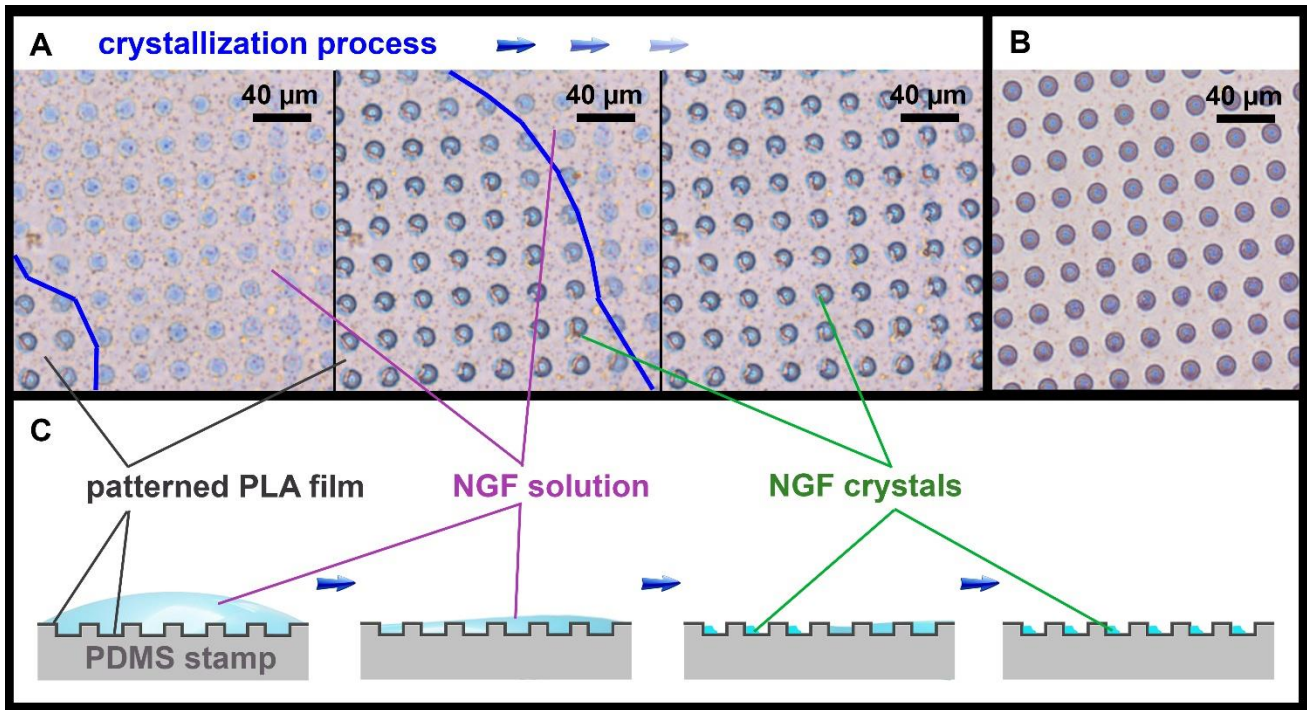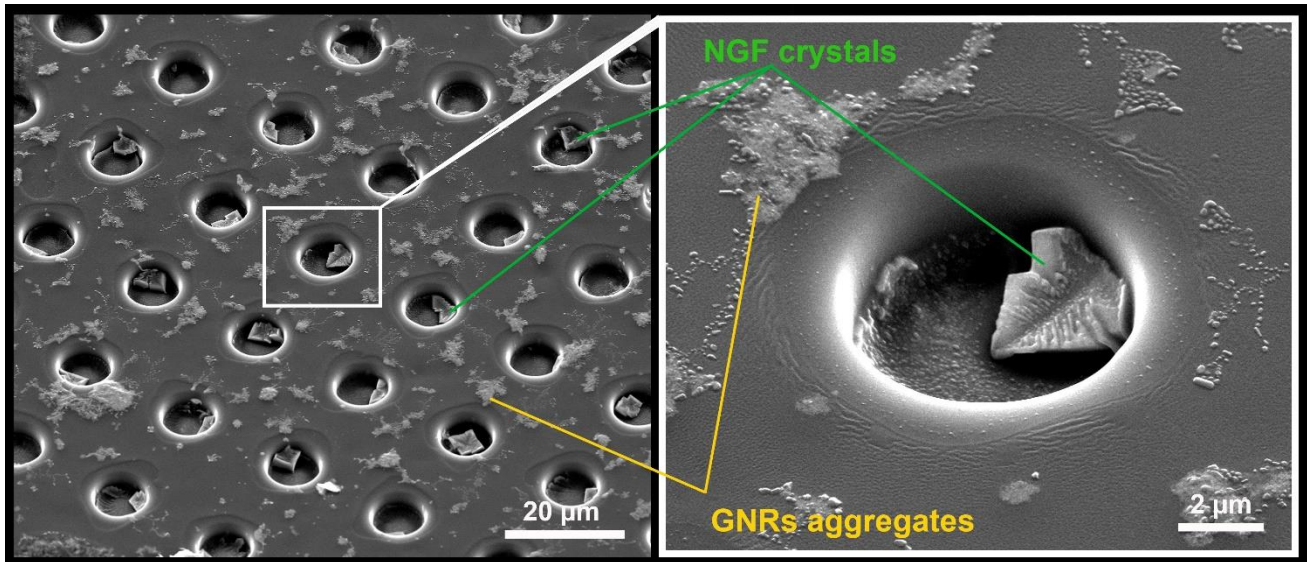
424

List of images

426

Figure 1. A diagram of the MCA, with a drug cargo and GNRs (A). Typical SEM image of PLA-based
MCA with GNRs (B). SEM images of PLA patterned film, without (C) and with GNR aggregates (D).
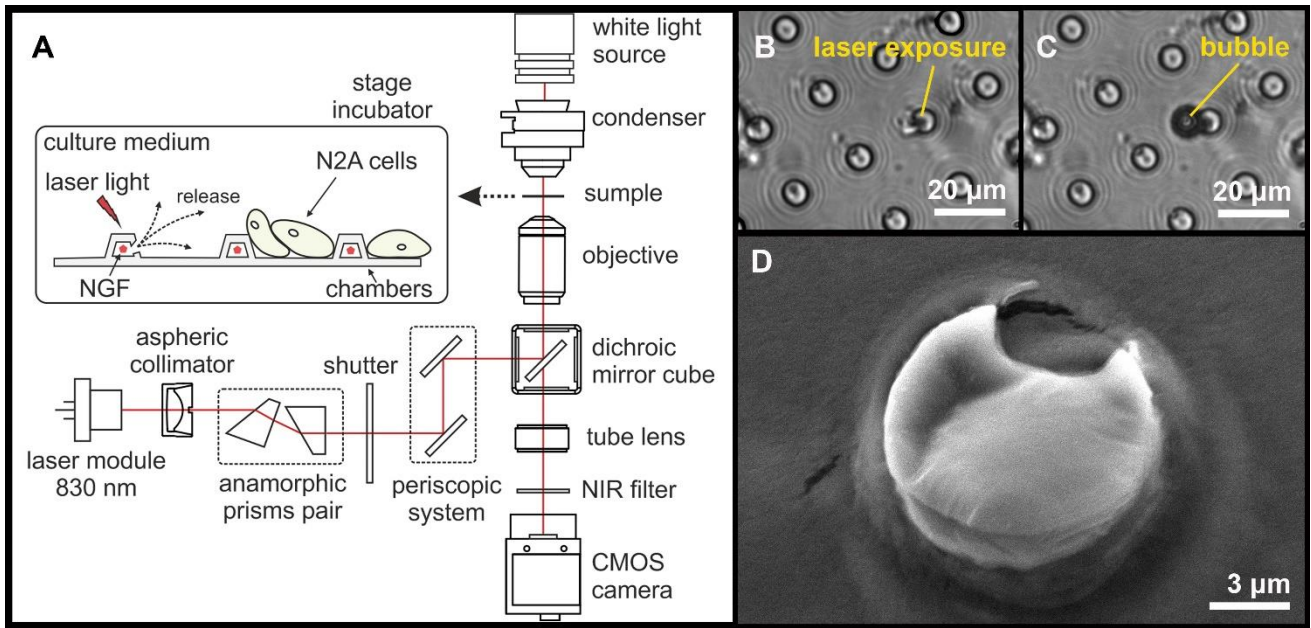The arrangement of GNR aggregates (E, TEM image).

Figure 2. Optical images of the patterned PLA film (A), showing the NGF crystallization process, and an empty patterned film (B), bright-field microscopy in phase contrast mode. The border of NGF solution drop is marked with a blue line. Schematic illustration of the NGF crystallization process on the patterned PLA film (C).
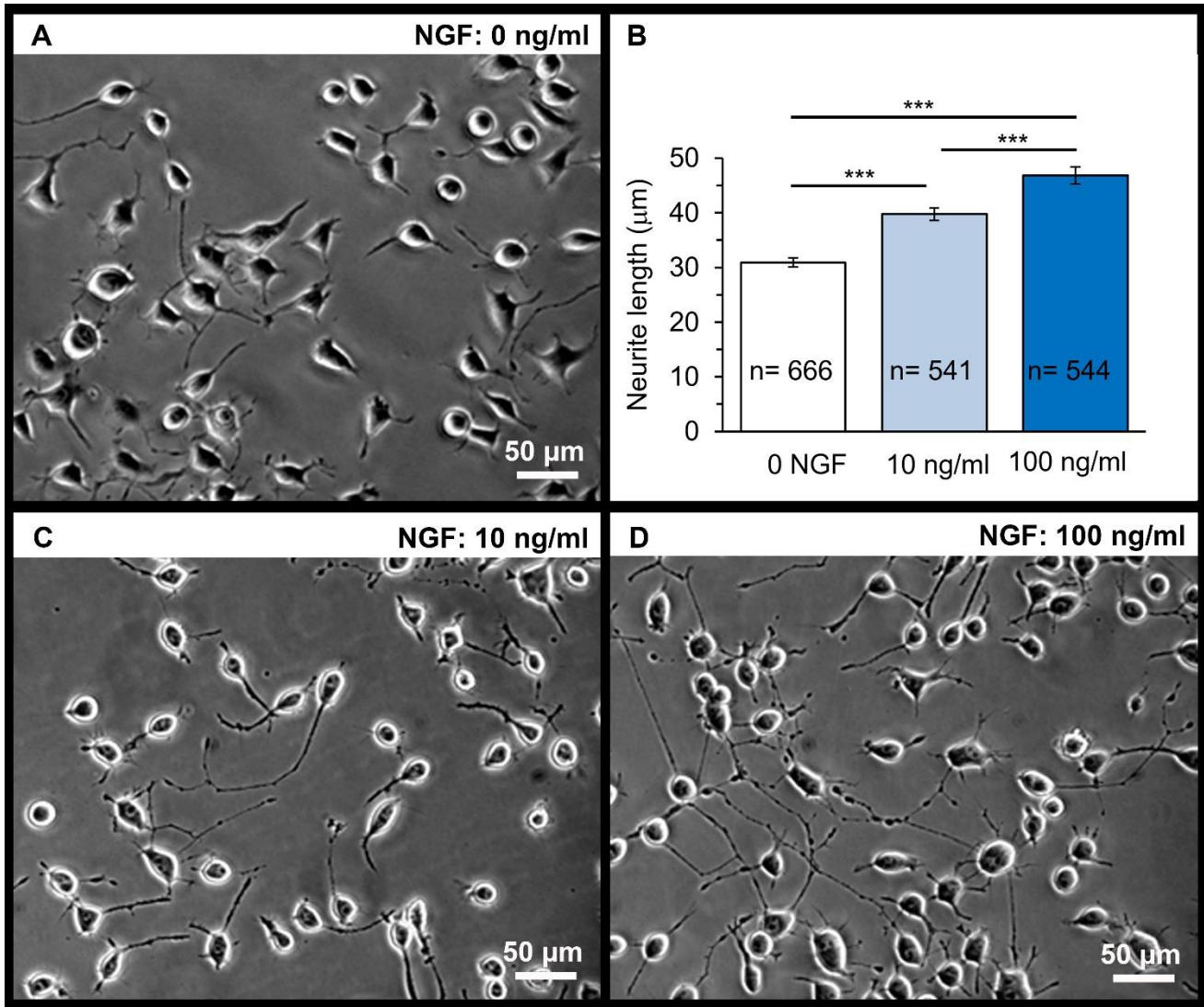

Figure 3. SEM images of NGF crystals inside the microwells on patterned PLA film.

437

Figure 4. A diagram illustrating the experimental design and the laser-induced opening of MCA with NGF loaded inside (A). Typical images of microchambers before (B) and after (C) laser exposure (bright-field microscopy). SEM image of an opened microchamber (D).

Figure 5. Dose-dependent effect of NGF on the neurite outgrowth in N2A cells on glass coverslips. A snapshot of differentiating N2A cells after 1 day of cell growth on glass (A). Statistical summary of the neurite length in N2A cells growing without or with NGF supplemented to culture medium at the concentration of 10 ng/ml or 100 ng/ml. Numbers of neurites measured for their length are indicated; at least four independent samples (coverslips) were tested for each group. ***P < 0.001 (two-tailed, unpaired t-test). (B) Representative images of differentiating N2A cells after 1 day of cell growth with NGF at different concentrations: 10 ng/ml (C) or 100 ng/ml (D).

449

450
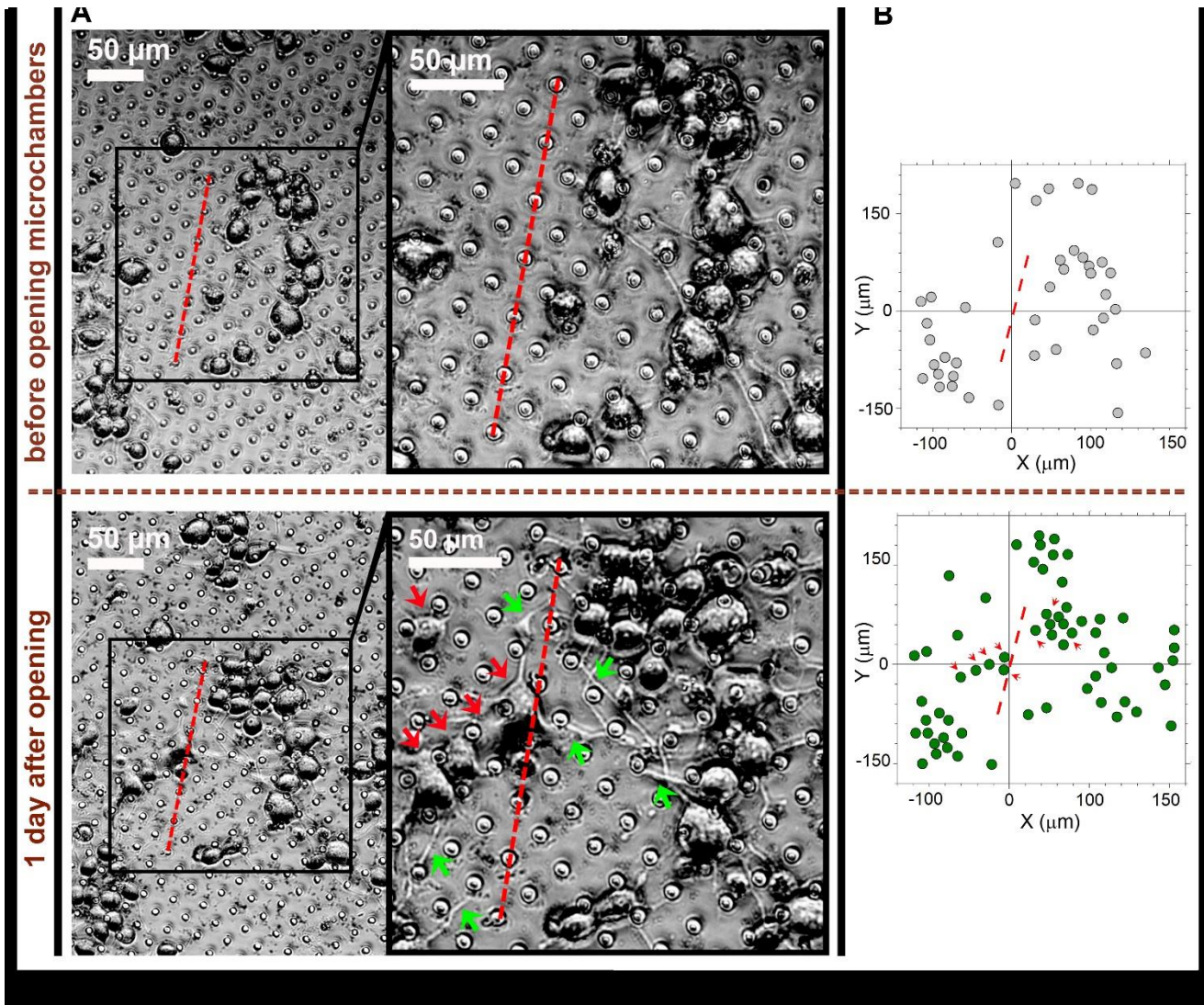
Figure 6. Directed neurite outgrowth by local N2A cells and cells migration towards the laser-opened microchambers with NGF payload inside. (A) Representative snapshots of differentiating N2A cells growing on the surface of PLA-based MCA with NGF payload inside microchambers before microchamber opening (upper row) and 1 day after (lower row). Red dotted line, a line segment trajectory for optical targeting microchambers (7 microchambers opened). Red arrows, directed migration of individual cells from their original positions; green arrows, cell neurites directed toward the opened microchambers (NGF release). (B) Cell tracking diagrams depicting individual N2A cell positions before laser-triggered microchamber opening (top) and 1 d after (bottom). Note directed migration of local cells (red arrows) from their original positions toward the opened microchambers. Data are representative of images on (A).

461
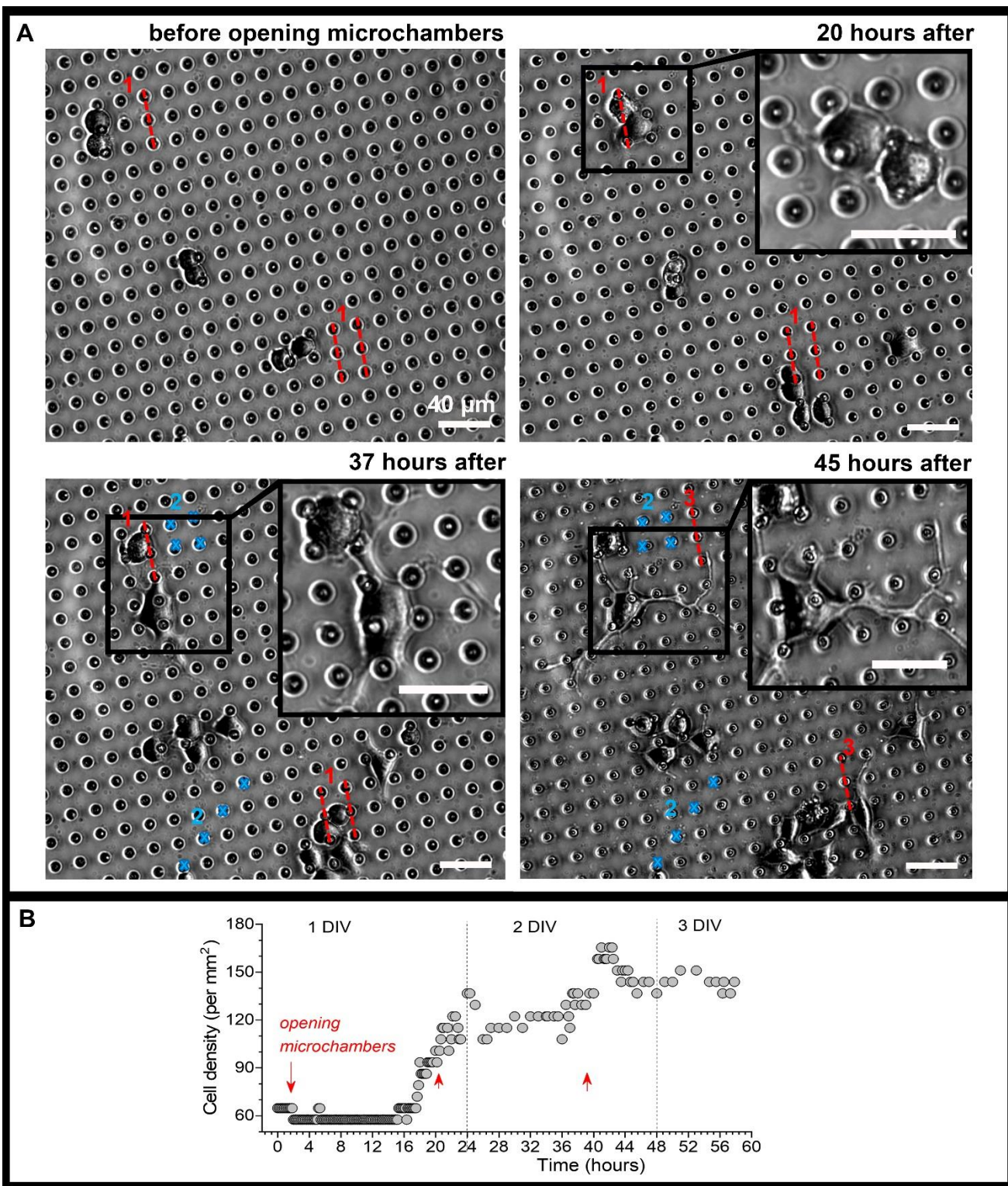
462

Figure 7. Monitoring morphogenesis of differentiating N2A cells upon triggered, site-specific NGF release from PLA-microchambers. (A) Representative snapshots of differentiating N2A cells on the surface of MCA with NGF-loaded microchambers before and following laser-triggered microchamber opening at various time-points. Images taken from the same area of interest; red dotted lines and blue marks, trajectories for optical targeting (the sequence consists of varied trajectory for opening 3 times,

468   ~20 hours apart). Scale bars, 40 μm. (B) Time-course of cell density changes within the targeted area
469   during the time-lapse imaging (~60 hours total) before and following triggered NGF release from PLA-
470   microchambers, shown on A. Red arrows, time of laser-triggered opening.

471